Applied Surface Science 430 (2018) 390–398

Contents lists available at ScienceDirect

Applied Surface Science

journal homepage: www.elsevier.com/locate/apsusc

Full Length Article

Photocatalytic performance of Cu-doped TiO_2 nanofibers treated by the hydrothermal synthesis and air-thermal treatment

Ming-Chung Wu[a,b,c,*], Po-Yeh Wu[a], Ting-Han Lin[a], Tz-Feng Lin[a,d]

[a] Department of Chemical and Materials Engineering, College of Engineering, Chang Gung University, Taoyuan 33302, Taiwan
[b] Green Technology Research Center, Chang Gung University, Taoyuan 33302, Taiwan
[c] Division of Neonatology, Department of Pediatrics, Chang Gung Memorial Hospital, Taoyuan 33305, Taiwan
[d] 3D Printing Medical Research Center, China Medical University Hospital, Taichung 40447, Taiwan

ARTICLE INFO

Article history:
Received 17 May 2017
Received in revised form 2 September 2017
Accepted 5 September 2017
Available online 6 September 2017

Keywords:
TiO_2
Metal ion doping
Nanofiber morphology
Phase transition
Photocatalysis
Hydrogen evolution

ABSTRACT

Series of transition metal-doped TiO_2 (metal/TiO_2) is prepared by combining the hydrothermal synthesis and air-thermal treatment without any reduction process. The selected transition metal precursors, including Ag, Au, Co, Cr, Cu, Fe, Ni, Pd, Pt, Y, and Zn, were individually doped into TiO_2 nanofibers to evaluate the photocatalytic degradation activity and photocatalytic hydrogen generation. Consider the photocatalytic performance of these synthesized metal/TiO_2 under UV-A irradiation, copper doped TiO_2 nanofibers (Cu/TiO_2 NFs) was chosen for further study due to its extraordinary reactivity. Systematical studies were spread to optimize the doping concentration and the calcination condition for much higher photocatalytic activity Cu/TiO_2 NFs. In the photocatalytic degradation test, 0.5 mol%-Cu/TiO_2 NFs calcined at 650 °C exhibits the highest activity, which is even higher than commercial TiO_2-AEROXIDE® TiO_2 P25 under UV-A irradiation. The synthesized 0.5 mol%-Cu/TiO_2-650 NFs also have the capability in the photocatalytic hydrogen production. The hydrogen evolution rates are 200 μmol/g·h under UV-A irradiation and 280 μmol/g·h under UV-B irradiation. The density of state calculated by CASTEP for Cu/TiO_2 indicates that Cu doping contributes to the states near valence band edge and narrows the band gap. The disclosed process in this study is industrial safe, convenient and cost-effective. We further produce a significant amount of TiO_2-based catalysts without any hydrogen reduction treatment.

© 2017 Elsevier B.V. All rights reserved.

1. Introduction

Photocatalysts have raised lots of attention because of its extensive applications in air purification [1–3], anti-bacteria [4–7], green energy [8–13], self-cleaning [14,15], water treatment [16], and CO_2 reduction [17–19]. The importance of photocatalyst in our daily life is its low cost, non-toxicity, chemical/thermal stability, ease of production and use, and being human- and environment-friendly [20,21]. In 1972, Honda and Fujishima discovered the water splitting phenomenon by using TiO_2 and platinum as the electrodes. Their pioneering works broaden TiO_2 photocatalytic studies and applications [22,23]. However, the wide bandgap of ~3.2 eV for anatase TiO_2 leads to little charge separation efficiency and the weak absorption under solar irradiation, which only utilizes ~5% UV radiation in the solar spectrum [24]. Many efforts have been made to overcome the TiO_2 bandgap issue toward a potential material. The visible or solar light photocatalytic activity of TiO_2 is enthusiastic to be demonstrated. The conventional method is metal or non-metal doping in the TiO_2 which generates the donor level or acceptor level in the forbidden band. The related bandgap and the best optoelectrical property thus shifted to the solar spectrum as designed.

Experienced scientists focused on the transition metal doping of TiO_2, and discussed the role of metal ion in electron-hole recombination dynamics [25]. The transition metal dopant such as Cu^{2+}, Fe^{3+}, Mn^{3+}, and Ni^{2+} adjusts not only the bandgap but also the behavior of electron-hole separation [26–35]. With decreasing the recombination probability of electron and hole, the oxidation-reduction reaction of transition metal-doped TiO_2 is enhanced a lot after visible light exposure. Based on this, when the transition metal Bi^{3+} and Ni^{2+} are well incorporated into TiO_2 lattice by the sol-gel method, it demonstrates the bandgap modulation so as to enrich the solar-light driven photocatalytic capability [28]. For Co^{2+}, Ni^{2+}, Mn^{3+}, and Cu^{2+} doped mesoporous TiO_2 film material, it exhibits a higher photocurrent efficiency than the non-doped mesoporous

* Corresponding author at: Department of Chemical and Materials Engineering, College of Engineering, Chang Gung University, Taoyuan 33302, Taiwan.
E-mail address: mingchungwu@mail.cgu.edu.tw (M.-C. Wu).

http://dx.doi.org/10.1016/j.apsusc.2017.09.035
0169-4332/© 2017 Elsevier B.V. All rights reserved.

TiO_2 film material [32]. As a result of the formation of larger surface area, Fe^{3+} doped TiO_2 produced by the hydrothermal method gives a higher photodegradation rate than the non-doped TiO_2 [33]. It is observed that the transition metal doped TiO_2 promotes the photocatalytic activity due to the decreased bandgap, the decreased recombination rate of electron and hole, and the increased specific surface area. Moreover, the computer calculation based on density functional theory of first-principles is helpful for investigation of the photocatalytic performance and mechanism. The band structure and electronic properties of metal doped TiO_2 can be accurately predicted [36,37].

Among various transition metals, it is noted that Cu^{2+}-doped TiO_2 has attracted many interests due to its low cost, high photocatalytic activity and possesses the ability of visible light absorption. Cu^{2+}-doped TiO_2 synthesized by the sol-gel method has the bandgap of 2.83 eV, and the Cu^{2+} acts as the electron trap that induces the electron-hole separation [38,39]. The radius of Cu^{2+} is a major factor for substantial substitutional solid solubility. According to the radius difference between Cu^{2+} (0.73 Å) and Ti^{4+} (0.61 Å) is less than 15%, Cu^{2+} can be doped into the TiO_2 lattice very easily. Therefore, for the substantial substitutional type, Cu^{2+} doping can generate the donor levels below the conduction band of TiO_2 and reasonably enhance the absorption behavior under visible light irradiation [38–41].

In this study, we began to synthesize a series of 1.0 mol% transition metal-doped TiO_2 by the hydrothermal method followed by an air-thermal treatment. The candidate transition metal includes Ag, Au, Co, Cr, Cu, Fe, Ni, Pd, Pt, Y, and Zn. The best transition metal-doped TiO_2 was found out to show the highest photocatalytic performance by measuring the photocatalytic activity. Considering the cost and the performance of each transition metal-doped TiO_2, Cu/TiO_2 was recommended as the best candidate for industrial usage. The optimized processing parameters for the high photoactivity of Cu/TiO_2 is reported in the manuscript. The crystalline structure, microstructure, absorption behavior, and photocatalytic activity are systematically studied to know the photocatalytic mechanism.

2. Experimental details

Eleven types of transition metal-doped TiO_2 were synthesized by the hydrothermal method. At first, 2.50 g TiO_2 anatase powder (Sigma-Aldrich, 98%) and various transition metal precursor were suspended in 62.5 mL sodium hydroxide aqueous solution (~10.0 M). The transition metal precursors are listed as follows: silver nitrate ($AgNO_3$, Choneye, 99.8 +%), hydrogen tetrachloroaurate(III) trihydrate ($HAuCl_4{\cdot}3H_2O$, Acros, 99.9%), cobalt(II) nitrate hexahydrate ($Co(NO_3)_2{\cdot}6H_2O$, Acros, 99%), chromium(III) nitrate nonahydrate ($Cr(NO_3)_3{\cdot}9H_2O$, Acros, 99%), copper(II) nitrate trihydrate ($Cu(NO_3)_2{\cdot}3H_2O$, Acros, 99%), iron(III) nitrate nonahydrate ($Fe(NO_3)_3{\cdot}9H_2O$, Acros, 98 +%), nickel(II) nitrate hexahydrate ($Ni(NO_3)_2{\cdot}6H_2O$, Acros, 99%), palladium(II) acetate ($C_4H_6O_4Pd$, Acros, 47.5%), platinum(II) acetylacetonate ($C_{10}H_{14}O_4Pt$, Acros, 98%), yttrium(III) nitrate hexahydrate ($Y(NO_3)_3{\cdot}6H_2O$, Acros, 99.9%), zinc nitrate hexahydrate ($Zn(NO_3)_2{\cdot}6H_2O$, Choneye, 97%). Reactants were transferred into a polytetrafluoroethylene-lined autoclave followed by a thermal treatment under the condition of 150 °C for 24 h. Various transition metal-doped sodium titanate ($Na_2Ti_3O_7$) were obtained. Then, 0.10 M hydrochloric acid (HCl, Sigma-Aldrich, 37%) was used to exchange the sodium ion for protons. Finally, the transition metal-doped sodium hydrogen titanate ($Na_xH_{2-x}Ti_3O_7$) was filtered and dried in air at 80 °C. To obtain the various transition metal-doped TiO_2 (metal/TiO_2), the metal-doped $Na_xH_{2-x}Ti_3O_7$ was calcined at different temperatures (500, 550, 600, 650 and 700 °C) for 12 h at 5 °C/min heating rate.

The Kubelka-Munk function spectra of various metal/TiO_2 was recorded by an UV/Vis spectrophotometer (JASCO, V-730, Japan) ranged from 300 to 800 nm. The crystal structures of the non-doped TiO_2 series and Cu/TiO_2 series were determined by the synchrotron X-ray diffractometer (13A1, Biomembrane Scattering Station, National Synchrotron Radiation Research Center). The synchrotron X-ray spectra were collected from 5° to 45° of 2θ with a scan rate of 0.02°/s, and its wavelength is ~1.025 Å. Raman scattering spectra of the non-doped TiO_2 and Cu/TiO_2 were measured by using a micro-Raman scattering spectroscopy system combined with an output power of 50 mW, 532 nm green laser (UniDRON, UniNanoTech). The laser beam was focused by the objective lens (Mag 50×, NA ≈ 0.55, Olympus), and the focused laser beam diameter is about several micrometers. The high-resolution microstructure and lattice images of Cu/TiO_2 were observed by a field-emission transmission electron microscope (JEOL, JEM-ARM200FTH, Japan). X-ray photoelectron spectroscopy spectra were measured and recorded by X-ray photoelectron spectrometer system (K-Alpha, Thermo Fisher Scientific) using micro-focused Al Ka X-ray source.

For the activity measurement of photocatalytic degradation, methyl orange (ACROS, pure) was chosen as a degradation target. In this photodegradation experiment, 133.3 mg/L metal/TiO_2 was dispersed well in 10.0 ppm methyl orange aqueous solution. The pH value of the mixture solution during degradation reaction is about 6.0. At the beginning of the photodegradation experiment, the suspensions were kept in the dark for 30 min regarding the adsorption equilibrium so that we are able to revoke the adsorption error. The temperature of the photodegradation measurement was controlled at 25 °C. The UV-A lamps (Sankyo Denki, G8T5BLB, λ_{max} ~ 352 nm, 8.0 W) were placed ~ 10.0 cm high above the reaction system. After UV-A irradiation, the suspension was centrifuged at 5000 rpm for 15 min. The UV–vis absorption spectra between 300 ~ 800 nm were applied to analyze the residual methyl orange. The characteristic peak of methyl orange is located at λ = 464 nm. According to the pre-established calibration curve, we can calculate its corresponding concentration. The photodegradation of organic dye using TiO_2-based catalyst usually followed Langmuir-Hinshelwood kinetics [42,43]. It can be mathematically simplified to a first-order kinetics in the early stage as described as $\ln(C_0/C_t) = kt$, where C_0 is the initial methyl orange concentration, C_t is the methyl orange concentration at the various time, and k and t are the apparent reaction rate constant and photodegradation time respectively. After plotting the logarithm of the C_t/C_0 as a function of time for the various catalysts, the slopes of each fitting lines are identified as photocatalytic reaction rate. The reaction rate constants of the various catalysts were further calculated as well.

The computational simulation is based on CASTEP using the software of Biovia Materials Studio (version 8.0.0.843). It is a quantum mechanics-based program designed particularly for solid-state materials science. Density functional theory and exchange-correlation potential are utilized in the calculation. Perdew-Burke-Ernzerhof (PBE) of Generalized Gradient Approximation(GGA) was chosen for the gradient-corrected function. The properties of TiO_2 and Cu/TiO_2, including band structure, the density of states (DOS), and absorption spectra, were also simulated. The model of TiO_2 and Cu/TiO_2 is a 3×3×1 supercell. Moreover, Norm Conserving was chosen in pseudopotentials due to its accuracy in predicting optical properties. The energy cutoff and k-point in the CASTEP calculation were set at 10.0 eV and 2 × 2 × 3.

Photocatalytic hydrogen generation test was carried out in the 2.0 L mixture of C_2H_5OH and H_2O (volume ratio of 50:50). Fifty milligrams Cu/TiO_2 was dispersed well in the mixture of C_2H_5OH and H_2O by an ultrasonic bath. Three kinds of light sources, including

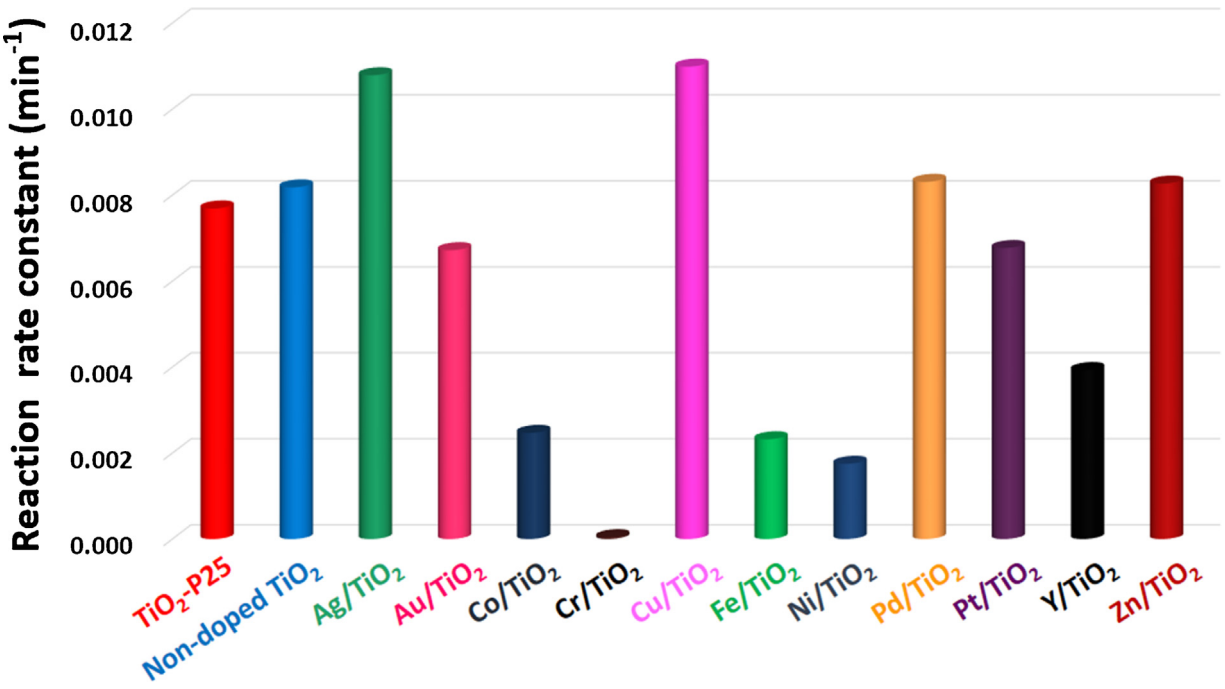

Fig. 1. The UV-A photodegradation reaction rate constants of TiO_2-P25, non-doped TiO_2, and 11 types of transient metal-doped TiO_2 NFs with 1.0 mol% doping concentration.

UV-B lamps (Sankyo Denki, G15T8E, $\lambda_{max} \sim 312$ nm, 8.0 W), UV–A lamps, and visible lamps (Goodly, F8T5/D, 8.0 W), were used in the photocatalytic hydrogen production measurement. The six lamps of various light sources were placed in a hexagonal arrangement around the reactor. Nitrogen gas (99.995%) was bubbled into the reaction system to avoid the sedimentation of Cu/TiO_2. Purging gas was also used for the evolving gaseous products. The nitrogen flow rate of 400 mL min^{-1} is controlled by a mass flow meter (C100L, Sierra). The liquid nitrogen cold trap system and the molecular sieve were connected to the outlet of the reaction system to diminish the vapor of C_2H_5OH and H_2O. Finally, the photocatalytic hydrogen generation rate was recorded by a Status FGD3 gas detector.

3. Results and discussion

Aiming to exploit photocatalyst for pollution treatment and green energy, highly photocatalytic performance in the organic compound degradation and hydrogen generation especially in the solar spectrum is the primary work for scientists. We propose a transition metal doping method in the TiO_2 to find out a new photocatalyst. Eleven types of transition metal-doped TiO_2 with a fixed doping concentration of 1.0 mol% calcined at 650 °C for 12 h were synthesized. They are denoted as Ag/TiO_2, Au/TiO_2, Co/TiO_2, Cr/TiO_2, Cu/TiO_2, Fe/TiO_2, Ni/TiO_2, Pd/TiO_2, Pt/TiO_2, Y/TiO_2 and Zn/TiO_2 NFs. A series of simple tests for photocatalytic degradation of methyl orange was applied to compare the activity of metal-doped TiO_2 NFs under UV-A irradiation. The photocatalytic decolorization phenomenon of various metal/TiO_2 is displayed by the bar chart of reaction rate constants as shown in Fig. 1. The photocatalytic activity of Cr/TiO_2 NFs shows approximately zero. In contrast, it is obviously noted that both Cu/TiO_2 and Ag/TiO_2 NFs exhibit outstanding performance and show the higher activity than TiO_2-P25 under UV–A irradiation. The reaction rate constants of Cu/TiO_2 and Ag/TiO_2 NFs are similar and related to 0.0109 min^{-1} and 0.0107 min^{-1}, respectively. Moreover, the cost of Cu precursor is lower than Ag precursor. These results are able to be summarized that Cu/TiO_2 is the best choice in cost and photocatalytic performance, and it could be an ideal candidate for the further study.

The series of the non-doped TiO_2-X and Cu/TiO_2-X NFs with 1.0 mol% doping concentration were calcined at several temperatures (inducing 500, 550, 600, 650 and 700 °C) in an air atmosphere for 12 h. The symbol "X" indicates the calcination temperature. It is the way to find the optimization of calcination process. The structural crystalline analysis of non-doped TiO_2-X NFs and Cu/TiO_2-X NFs series were obtained by a synchrotron X-ray diffractometer (**Fig. S1** and Fig. 2**(a)**). Non-doped TiO_2-650 NFs possesses the strongest crystalline of anatase TiO_2. As calcination temperature is up to 700 °C, rutile TiO_2 phase starts to grow in the anatase phase of pristine TiO_2. While Cu/TiO_2 NFs calcined at 500, 550, and 600 °C exhibit the characteristic peaks at 2θ around 18.94°, 19.75°, and 22.01°, and the characteristic peaks are identified as the phase of β-TiO_2 monoclinic [44]. When the calcination temperature goes to 650 °C, the characteristic peaks of β-TiO_2 transform into anatase TiO_2 phase. The diffraction peaks of Cu/TiO_2-X NFs series is consistent with the pristine anatase TiO_2 below 650 °C. The lattice parameters are the tetragonal crystal system with a = 3.78 Å and c = 9.51 Å. In contrast to the non-doped TiO_2, Cu/TiO_2 NFs show no rutile phase when the calcination temperature is achieved to 700 °C. The results suggest that the art of Cu doping into TiO_2 could hinder the formation of rutile TiO_2. The crystallite size of the non-doped TiO_2 and Cu/TiO_2 NFs series were calculated by Debye-Scherrer formula as shown in Fig. 2(b) [45]. With increasing of the calcination temperature, the crystallite size of the non-doped TiO_2 decreased due to the existence of rutile phase when the calcination temperature is above 650 °C. It is interesting to know that the crystallite size of Cu/TiO_2 NFs series become larger at high calcination temperature. The crystallinity and the crystallite size is also enhanced as well up to 700 °C. Therefore, we can see that Cu doping is a beneficial factor for improving the crystallinity of TiO_2. These results are notably unique than other metal doping TiO_2 nanomaterial such as bismuth and niobium in our previous study [35,46]. Generally, the crystalline of Bi-doped TiO_2 NFs significantly decreases with increasing doping concentration owing to destruction of anatase TiO_2 lattice by bismuth ion, and the Bi_2O_3 phase will form when the doping concentration is higher than 10.0 mol%. Niobium doping in TiO_2 crystalline also shows the smaller crystallite size with

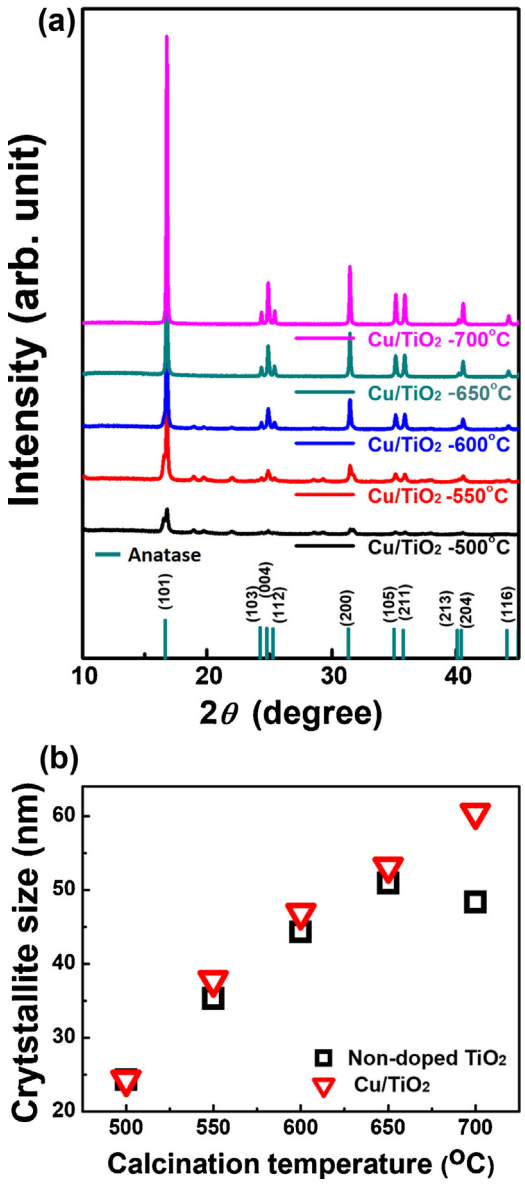

Fig. 2. (a) Synchrotron X-ray diffraction patterns of Cu/TiO_2 NFs series and **(b)** the calculated crystallite size of the non-doped TiO_2 and Cu/TiO_2 NFs.

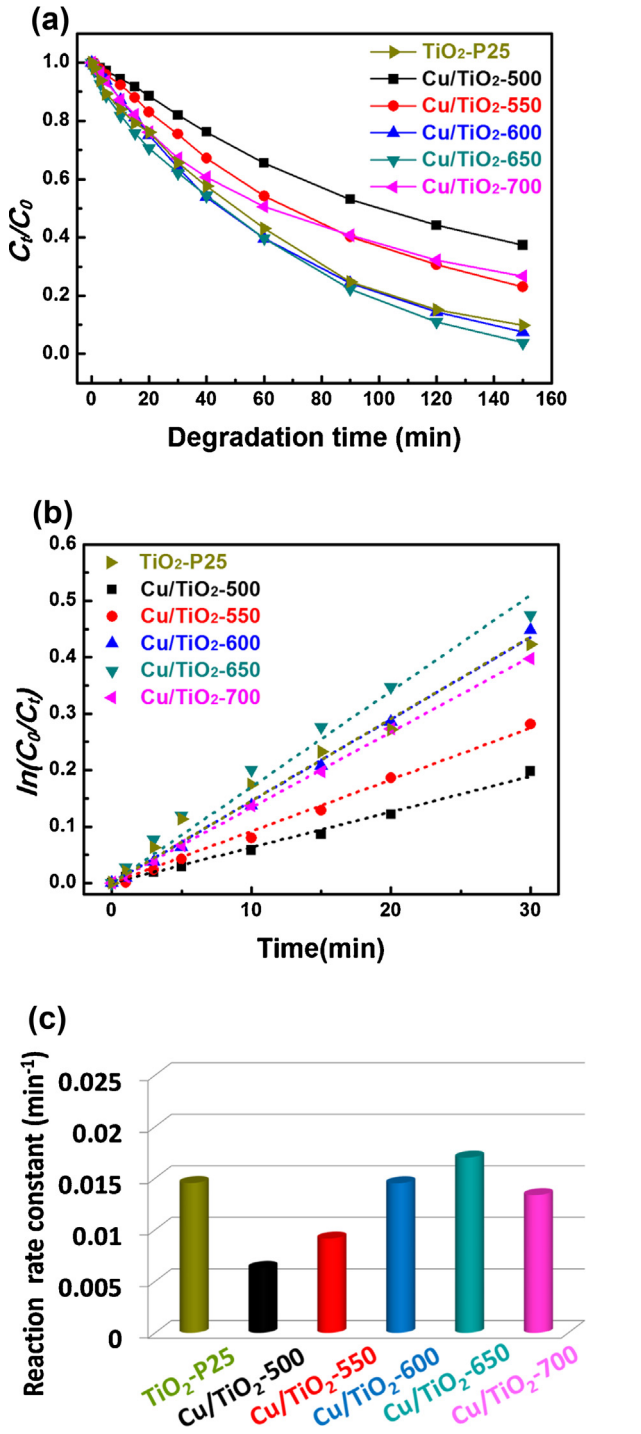

Fig. 3. (a) The C_t/Co curves, (b) the linearized kinetic plots, and **(c)** the reaction rate constants of the photocatalytic degradation of organic dye (i.e., methyl orange) under UV-A irradiation using various Cu/TiO_2 NFs calcined at the different temperatures and TiO_2-P25 as a comparison. (For interpretation of the references to colour in this figure legend, the reader is referred to the web version of this article.)

increasing the doping concentration, but it will not form the new phase.

The correlation between the calcination temperature and the photocatalytic activity for Cu/TiO_2 NFs was discussed by the photodegradation experiments of methyl orange. The standard material TiO_2-P25 was acted as the comparison basis in the photodegradation test. For the photodegradation measurement, the color expression of the solution is changed from initial orange to colorless. It typically follows the Langmuir-Hinshelwood kinetics [42,43]. The C_t/C_0 curves of Cu/TiO_2-X NFs series from the photodegraded methyl orange under UV-A irradiation is shown in Fig. 3(a). Plotting the logarithm of the C_t/C_0 as a function of time, we acquired the corresponding linear slopes for Cu/TiO_2-X NFs series as shown in Fig. 3(b). The reaction rate constant for the photodegradation of Cu/TiO_2-X series is shown using bar chart in Fig. 3(c). Cu/TiO_2-650 NFs displays the highest reaction rate among Cu/TiO_2-X NFs series. It is even higher than TiO_2-P25. The optimal calcination temperature of 650 °C is therefore suggested for synthesis process.

After discovering the optimal parameter of calcination process, we synthesized a series of Cu/TiO_2-650 NFs with several doping concentrations and characterized them by synchrotron X-ray diffractometer. Synchrotron X-ray diffraction pattern of Cu/TiO_2-650 NFs with doping concentrations involving 0.5, 1.0, 3.0, 5.0, and 10.0 mol% are shown in Fig. 4(a). There is no phase transformation happened as the increasing of doping concentration. We suggest that the art of doping Cu into TiO_2 material does not alter the crystalline structure of anatase TiO_2, even the doping concentration up to 10.0 mol%. The results can be attributed to the similar ionic

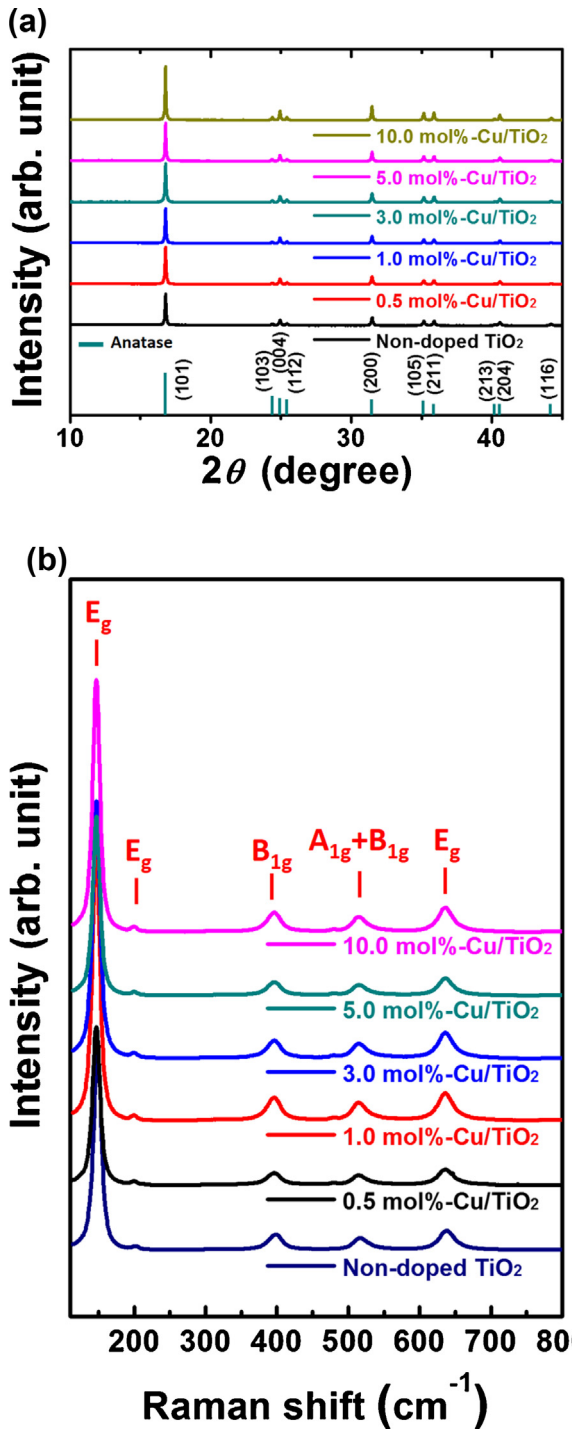

Fig. 4. (a) Synchrotron X-ray diffraction patterns and (b) Raman spectra of Cu/TiO_2-650 NFs series with several doping concentrations.

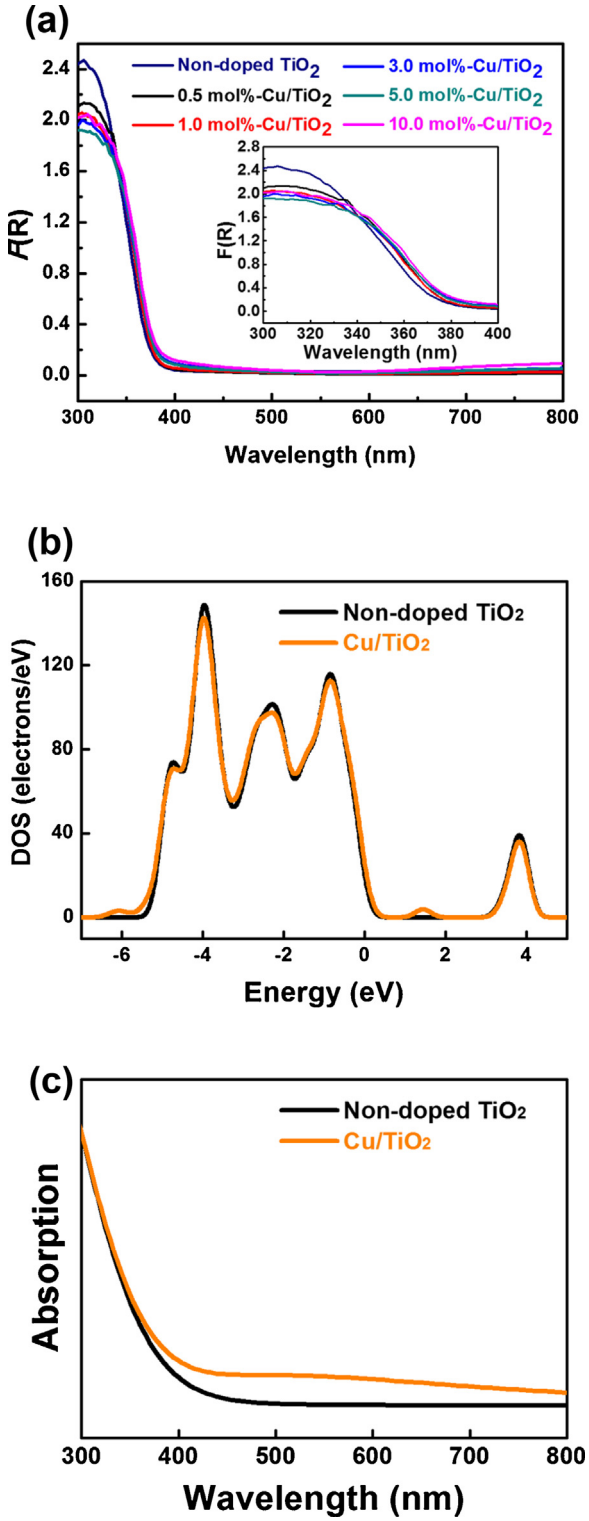

Fig. 5. (a) The Kubelka–Munk function of Cu/TiO_2-650 NFs series with different doping concentrations, (b) density of states (DOS), and (c) simulated absorption of the non-doped TiO_2 and Cu/TiO_2 NFs.

radius of Cu ion and Ti^{4+} [12,17,47,48]. Raman spectroscopy was also applied to investigate the crystal structure of Cu/TiO_2-650 NFs series (Fig. 4(b)). The Raman peaks at 146.8 (E_g), 199.6 (E_g), 397.9 (B_{1g}), 513.0 (A_{1g}), 518.9 (B_{1g}), and 637.2 (E_g) cm^{-1} mainly indicated the anatase TiO_2, and they are corresponding to the six symmetric Raman-active modes [49]. The superimposed phenomenon occurs at 513.0 and 518.9 cm^{-1}. Thus it shows a broad peak at 515.9 cm^{-1}. When the Cu doping concentration is less than 10.0 mol%, the intensity of the Raman scattering is proportional to the copper doping concentration. The increased copper doping improves the crystal structure of anatase TiO_2. The Raman spectrum supports the conclusion from the synchrotron XRD pattern. There is no phase transformation of crystal structure while Cu dopant is in the TiO_2 NFs.

The Kubelka–Munk function (F(R)) spectra of Cu/TiO_2 NFs series with various doping concentration were observed as shown in Fig. 5**(a)**. The F(R) plot gives a correlation between the reflectance and the Cu doping concentrations [50]. It is noted that there is a

slight redshift between 300 and 400 nm. Fig. 5**(b)** shows the density of state (DOS) of the non-doped TiO_2 and Cu/TiO_2 NFs that is calculated by the gradient-corrected functional (GGA-PBE) of CASTEP. The 3*d* orbital of Ti and the 2*p* orbital of O exists in the valence band and the conduction band of TiO_2 as shown in **Fig. S2**. The valence band is mainly attributed to the Ti 3*d* orbital and the partial of O 2*p* orbital. On the other hand, the conduction band is dominated by the 2*p* orbital of O. A mid-bandgap is formed between the valence band and conduction band when the Cu is doped into TiO_2. The simulated absorption spectra show that the non-doped TiO_2 only exists the absorption in UV band as shown in Fig. 5**(c)**. Once the Cu was doped into TiO_2, it can absorb visible light due to the existent of Cu 3*d* orbital which is consistent with the experiments we had made.

Further, we measured the photodegradation activity of Cu/TiO_2-650 NFs series to understand the doping effect of the light exposure. Under UV-A irradiation, 0.5 mol%-Cu/TiO_2-650 exhibits the highest degradation rate as shown in Fig. 6(a) and (b). We calculated the reaction rate constants of various Cu/TiO_2 NFs samples as the bar chart in Fig. 6(c). The reaction rate constant of 0.5 mol%-Cu/TiO_2-650 NFs is 0.018 min^{-1} that is higher than 0.007 min^{-1} of TiO_2-P25. It is interesting to know that when the Cu doping concentration is higher than 1.0 mol%, the photocatalytic activity is decreased with increasing the doping concentration. The result is due to the high concentration of Cu dopant could trap the electrons in the TiO_2 lattice so as to reduce the separation of electron and hole [51].

Another strategy, photocatalytic hydrogen production is often applied to evaluate the activity of photocatalysts. For non-doped TiO_2, it shows an undetectable value of photocatalytic hydrogen production under various light sources. The water splitting and hydrogen generation is a typical uphill reaction. The reaction will not occur when the energy of a photon is smaller to the band gap of the TiO_2. In Fig. 6, 0.5 mol%-Cu/TiO_2-650 NFs possesses the highest decolorization rate among all TiO_2-based materials. The optimal photocatalyst, 0.5 mol%-Cu/TiO_2-650 NFs, is tested to investigate the feasibility of hydrogen production. The photocatalytic hydrogen production rates of 0.5 mol%-Cu/TiO_2-650 NFs under various irradiation sources are shown in Fig. 7. Under visible light irradiation, the hydrogen detector showed an undetectable value caused by the insufficient energy of visible light. It is due to the excited photon with the limited energy that is smaller than Cu/TiO_2 bandgap which is unable to create the electron-hole pair. On the other hand, the hydrogen production rates under UV-A and UV-B irradiation can reach ~200 μmol/g·h and ~280 μmol/g·h, respectively. The photostability test of methyl orange with 0.5 mol%-Cu/TiO_2 NFs under UV-B light was shown in **Fig. S3** of supporting information. After five recycling of photodegradation, 0.5 mol%-Cu/TiO_2 NFs still maintained great photocatalytic activity.

The chemical compositions of non-doped TiO_2 and 0.5 mol%-Cu/TiO_2-650 were analyzed by XPS as shown in **Fig. S4**, and the results of XPS are summarized in Table 1. XPS survey spectrum of 0.5 mol%-Cu/TiO_2-650 is shown in **Fig. S4(a)**. The Ti^{4+} $2p_{1/2}$ and Ti^{4+} $2p_{3/2}$ for 0.5 mol%-Cu/TiO_2-650 are located at binding energy of 464.2 and 458.5 eV, respectively. For the O *1 s* spectrum, four O *1 s* peaks are contributed to lattice oxygen of TiO_2 the (529.7 eV), Cu_2O (530.5 eV), CuO (530.7 eV), and OH group (531.5 eV). In **Fig. S4(d)**, The Cu concentration of 0.5 mol%-Cu/TiO_2-650 NFs is ~0.33 at.%. The Cu ion existing with the chemical state of Cu^+ and Cu^{2+} at the binding energy around 932.1 and 933.1 eV, respectively. Due to the proper conduction band edges of CuO (-0.96 V) and Cu_2O (-0.22 V), Cu dopant is the best candidate to enhance H_2 generation [52].

The microstructure of Cu/TiO_2 NFs is a strong factor that would affect the photocatalytic activity. TEM was applied to observe the microstructure of 0.5 mol%-Cu/TiO_2-650 NFs (Fig. 8). From TEM image as shown in Fig. 8**(a)**, the synthesized 0.5 mol%-Cu/TiO_2-650 NFs is present as a linear, uniform and separated fiber morphology. One dimension Cu-doped TiO_2 Nanofibers can promote the electron mobility and exhibit the excellent charge separation ability so that it can reduce the recombination of electron and hole [53]. The synthesized 0.5 mol%-Cu/TiO_2-650 NFs in this study is reasonable to show a higher photocatalytic activity than the other

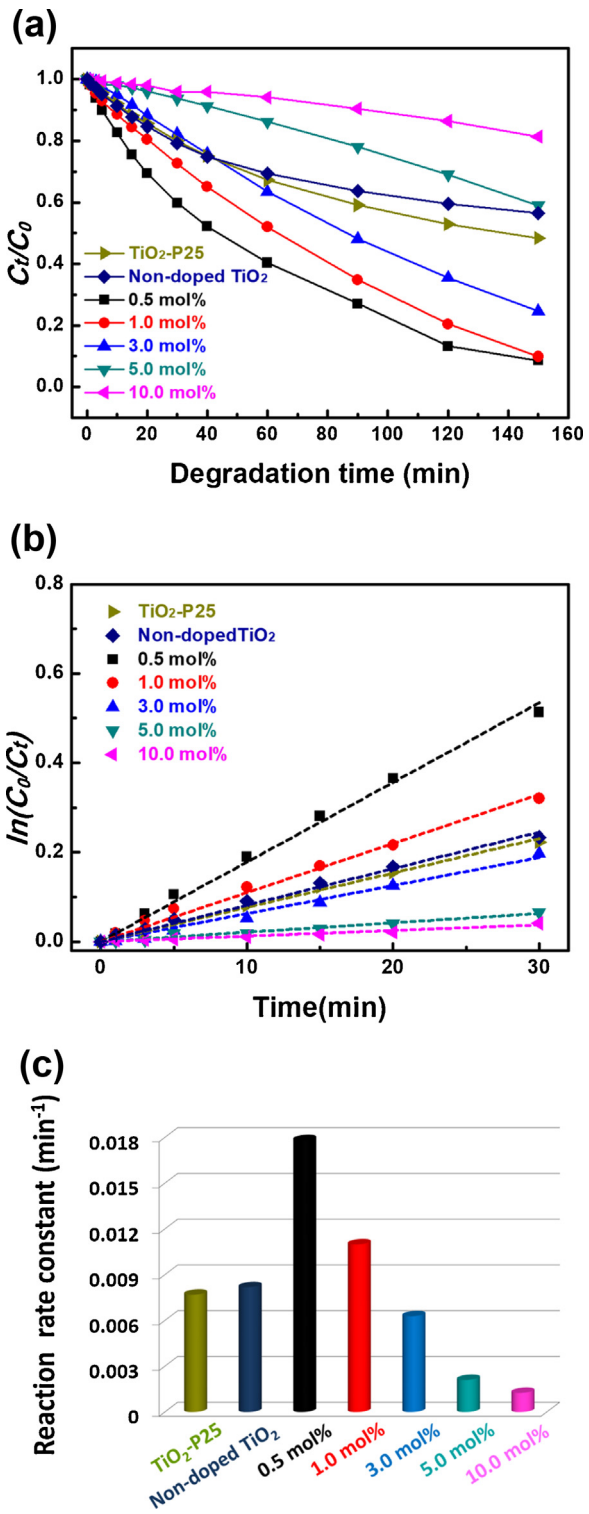

Fig. 6. (a) The C_t/Co curves, (b) the linearized kinetic plots, and (c) the reaction rate constants of the photocatalytic degradation of methyl orange under UV-A irradiation using various Cu/TiO_2 NFs with different doping concentration and TiO_2-P25. (For interpretation of the references to colour in this figure legend, the reader is referred to the web version of this article.)

Table 1
Results of XPS analysis of non-doped TiO_2 and Cu/TiO_2 NFs.

Material	Ti $2p_{3/2}$		O 1s		Cu 2p	
	BE (eV)	Conc. (at.%)	BE (eV)	Conc. (at.%)	BE (eV)	Conc. (at.%)
Non-doped TiO_2 NFs	458.5	30.45	529.7	69.55	Not detected	
Cu/TiO_2 NFs	458.5	30.26	529.7	69.41	932.4	0.33

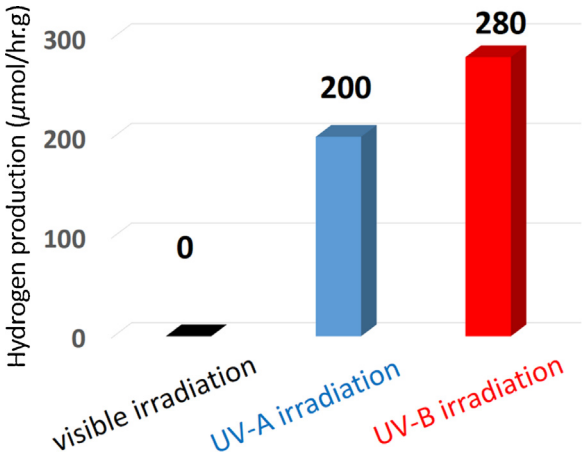

Fig. 7. The photocatalytic hydrogen production rates of 0.5 mol%-Cu/TiO_2-650 under the different light sources irradiation.

shapes/morphology. The high-magnification lattice image with the corresponding fast-Fourier-transformed pattern of 0.5 mol%-Cu/TiO_2-650 NFs is shown in Fig. 8(b). High-resolution TEM image illustrates that 0.5 mol%-Cu/TiO_2-650 NFs exhibits a high crystallinity and the $d_{(101)}$ is 3.43 Å which is slightly larger than 3.41 Å of non-doped TiO_2 [54]. The result may be due to the ionic radius of Cu^+ (0.77 Å) is larger than Ti^{4+} (0.61 Å).

The mechanism of photodegradation of organic dye by using Cu/TiO_2 NFs is shown in Fig. 9. Since the energy of irradiation source is higher than the intrinsic bandgap of TiO_2, the electron-hole pair will be generated. Once the electron (e^-) and hole (h^+) migrates to the surface of Cu/TiO_2 where the organic compounds absorbed on, the hole will react with water (H_2O) and hydroxide ions (OH^-) to form the proton (H^+) and the hydroxyl radicals ($OH^\bullet$). In addition, the electron and oxygen (O_2) will go through a reaction to form superoxide ion ($O_2^{-\bullet}$). The superoxide ion with excellent reducing ability will react with a proton to generate hydroperoxyl radical ($HO_2^\bullet$). The free radicals usually show the strong oxidizing ability. They can react with the organic compound adsorbed on Cu/TiO_2 NFs surface. After a series of oxidation-reduction reactions, the organic compound will be oxidized into the environmental friendly compounds, such as water and carbon dioxide. The developed Cu/TiO_2 NFs in this study is a high-performance and cost-effective material. It would be useful for the removal of pollutants from water and wastewater.

4. Conclusion

The eleven types of transition metals, including Ag, Au, Co, Cr, Cu, Fe, Ni, Pd, Pt, Y, and Zn, were doped into TiO_2 respectively to enhance the photocatalytic performance. Systematic studies were made to conclude an optimized processing method for Cu/TiO_2 NFs. Cu doping could hinder the phase transformation from anatase to rutile while increasing the calcination temperature. The photocatalytic hydrogen production rates by using 0.5 mol%-Cu/TiO_2-650 are ~200 μmol/g·h under UV-A irradiation and ~280 μmol/g·h under UV-B irradiation. For the photodegradation test under UV-A irradiation, Cu/TiO_2 NFs exhibits the fastest decolonization rate.

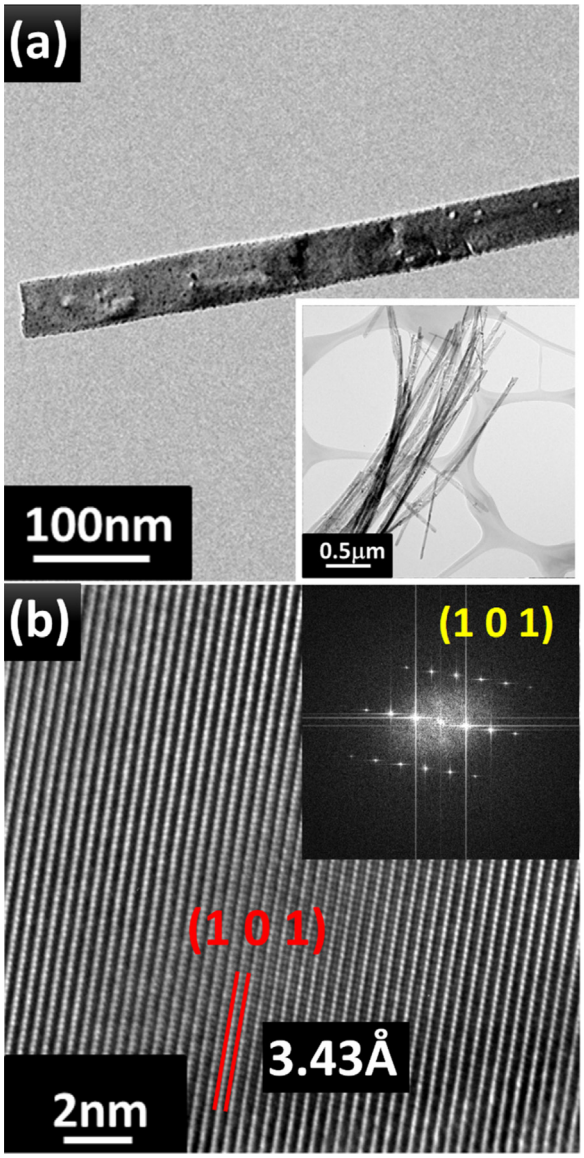

Fig. 8. (a) TEM images and (b) high-magnification lattice image of 0.5 mol% Cu/TiO_2 NFs calcined at 650 °C for 12 h.

For the photodegradation test under visible light irradiation, the reaction rate constant of 0.5 mol%-Cu/TiO_2-650 is 0.018 min^{-1} that higher than 0.007 min^{-1} of TiO_2-P25. The result illustrates a soft controlling of the heterophase junction and highly crystalline anatase TiO_2, and it may strongly improve the photocatalytic activity for the TiO_2-based materials.

Acknowledgements

The authors appreciate Prof. Wei-Fang Su at National Taiwan University,and Dr. Ming-Tao Lee at National Synchrotron Radiation Research Center (BL-13A1). The authors acknowledge the financial support from Ministry of Science and Technology of

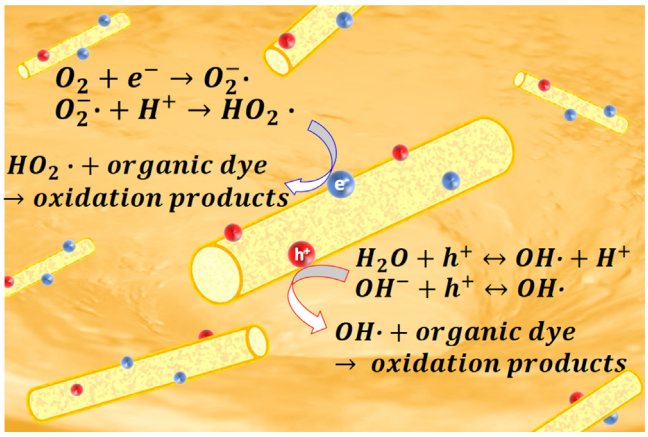

Fig. 9. The photodegradation mechanism of methyl orange for the Cu/TiO_2 NFs. (For interpretation of the references to colour in this figure legend, the reader is referred to the web version of this article.)

Taiwan (MOST 106-2119-M-002-030, MOST 106-2221-E-182-057-MY3, and MOST 106-2632-E-182-001) and Chang Gung Memorial Hospital, Linkou (CMRPD2E0071, CMRPD2E0072 and BMRPC74).

Appendix A. Supplementary data

Supplementary data associated with this article can be found, in the online version, at http://dx.doi.org/10.1016/j.apsusc.2017.09.035.

References

[1] G. Zhang, Z. Sun, Y. Duan, R. Ma, S. Zheng, Synthesis of nano-TiO2/diatomite composite and its photocatalytic degradation of gaseous formaldehyde, Appl. Surf. Sci. 412 (2017) 105–112.
[2] S. Weon, W. Choi, TiO2 nanotubes with open channels as deactivation-resistant photocatalyst for the degradation of volatile organic compounds, Environ. Sci. Technol. 50 (2016) 2556–2563.
[3] D. Li, H. Haneda, S. Hishita, N. Ohashi, Visible-light-driven N-F-Codoped TiO2 photocatalysts. 2. optical characterization photocatalysis, and potential application to air purification, Chem. Mater. 17 (2005) 2596–2602.
[4] J. Xu, X. Zhou, Z. Gao, Y.-Y. Song, P. Schmuki, Visible-light-triggered drug release from TiO2 nanotube arrays: a controllable antibacterial platform, Angew. Chem. 128 (2016) 603–607.
[5] J.C. Yu, W. Ho, J. Lin, H. Yip, P.K. Wong, Photocatalytic activity antibacterial effect, and photoinduced hydrophilicity of TiO2 films coated on a stainless steel substrate, Environ. Sci. Technol. 37 (2003) 2296–2301.
[6] S. Ma, S. Zhan, Y. Jia, Q. Zhou, Superior antibacterial activity of Fe3O4-TiO2 nanosheets under solar light, ACS Appl. Mater. Interfaces 7 (2015) 21875–21883.
[7] G. Villatte, C. Massard, S. Descamps, Y. Sibaud, C. Forestier, K.-O. Awitor, Photoactive TiO2 antibacterial coating on surgical external fixation pins for clinical application, Int. J. Nanomed. 10 (2015) 3367–3375.
[8] M.-C. Wu, W.-C. Chen, T.-H. Lin, K.-C. Hsiao, K.-M. Lee, C.-G. Wu, Enhanced open-circuit voltage of dye-sensitized solar cells using Bi-doped TiO2 nanofibers as working electrode and scattering layer, Sol. Energy 135 (2016) 22–28.
[9] M.-C. Wu, S.-H. Chan, M.-H. Jao, W.-F. Su, Enhanced short-circuit current density of perovskite solar cells using Zn-doped TiO2 as electron transport layer, Sol. Energy Mater. Sol. Cells 157 (2016) 447–453.
[10] F. Giordano, A. Abate, J.P. Correa Baena, M. Saliba, T. Matsui, S.H. Im, S.M. Zakeeruddin, M.K. Nazeeruddin, A. Hagfeldt, M. Graetzel, Enhanced electronic properties in mesoporous TiO2 via lithium doping for high-efficiency perovskite solar cells, Nat. Commun. 7 (2016) 10379.
[11] M.A. Mejía Escobar, S. Pathak, J. Liu, H.J. Snaith, F. Jaramillo, ZrO2/TiO2 electron collection layer for efficient meso-superstructured hybrid perovskite solar cells, ACS Appl. Mater. Interfaces 9 (2017) 2342–2349.
[12] D. Ni, H. Shen, H. Li, Y. Ma, T. Zhai, Synthesis of high efficient Cu/TiO2 photocatalysts by grinding and their size-dependent photocatalytic hydrogen production, Appl. Surf. Sci. 409 (2017) 241–249.
[13] Q. Hu, J. Huang, G. Li, J. Chen, Z. Zhang, Z. Deng, Y. Jiang, W. Guo, Y. Cao, Effective water splitting using CuOx/TiO2 composite films: role of Cu species and content in hydrogen generation, Appl. Surf. Sci. 369 (2016) 201–206.
[14] A. Khataee, L. Moradkhannejhad, V. Heydari, B. Vahid, S.W. Joo, Self-cleaning acrylic water-based white paint modified with different types of TiO2 nanoparticles, Pigm. Resin Technol. 45 (2016) 24–29.
[15] G. Doganli, B. Yuzer, I. Aydin, T. Gultekin, A.H. Con, H. Selcuk, S. Palamutcu, Functionalization of cotton fabric with nanosized TiO2 coating for self-cleaning and antibacterial property enhancement, J. Coat. Technol. Res. 13 (2016) 257–265.
[16] J. Singh, K. Sahu, A. Pandey, M. Kumar, T. Ghosh, B. Satpati, T. Som, S. Varma, D.K. Avasthi, S. Mohapatra, Atom beam sputtered Ag-TiO2 plasmonic nanocomposite thin films for photocatalytic applications, Appl. Surf. Sci. 411 (2017) 347–354.
[17] M. Tahir, B. Tahir, Dynamic photocatalytic reduction of CO2 to CO in a honeycomb monolith reactor loaded with Cu and N doped TiO2 nanocatalysts, Appl. Surf. Sci. 377 (2016) 244–252.
[18] C. Liu, S.K. Iyemperumal, N.A. Deskins, G. Li, Photocatalytic CO2 reduction by highly dispersed Cu sites on TiO2, J. Photonics Energy 7 (2016), 012004–012004.
[19] J. Low, B. Cheng, J. Yu, Surface modification and enhanced photocatalytic CO2 reduction performance of TiO2: a review, Appl. Surf. Sci. 392 (2017) 658–686.
[20] M.-C. Wu, Y.-H. Chang, T.-H. Lin, Bismuth doping effect on crystal structure and photodegradation activity of Bi–TiO2 nanoparticles, Jpn. J. Appl. Phys. 56 (2017) 04CJ01.
[21] J. Zhang, P. Zhou, J. Liu, J. Yu, New understanding of the difference of photocatalytic activity among anatase, rutile and brookite TiO2, Phys. Chem. Chem. Phys. 16 (2014) 20382–20386.
[22] A. Fujishima, K. Honda, Electrochemical Photolysis of water at a semiconductor electrode, Nature 238 (1972) 37–38.
[23] S.G. Kumar, K.S.R.K. Rao, Comparison of modification strategies towards enhanced charge carrier separation and photocatalytic degradation activity of metal oxide semiconductors (TiO2, WO3 and ZnO), Appl. Surf. Sci. 391 (2017) 124–148.
[24] J. Liu, Q. Zhang, J. Yang, H. Ma, M.O. Tade, S. Wang, J. Liu, Facile synthesis of carbon-doped mesoporous anatase TiO2 for the enhanced visible-light driven photocatalysis, Chem. Commun. 50 (2014) 13971–13974.
[25] A.T. Wonyong Choi, Michael R. Hoffmann, The role of metal ion dopants in quantum-sized TiO2: Correlation between photoreactivity and charge carrier recombination dynamics, J. Phys. Chem. C 98 (1994) 13669–13679.
[26] L.G. Devi, S.G. Kumar, Influence of physicochemical?electronic properties of transition metal ion doped polycrystalline titania on the photocatalytic degradation of Indigo Carmine and 4-nitrophenol under UV/solar light, Appl. Surf. Sci. 257 (2011) 2779–2790.
[27] H.P. Jina Choi, Michael R. Hoffmann, Effects of single metal-ion doping on the visible-light photoreactivity of TiO2, J. Phys. Chem. C 114 (2010) 783–792.
[28] V. Bhatia, A. Dhir, Transition metal doped TiO2 mediated photocatalytic degradation of anti-inflammatory drug under solar irradiations, J. Environ. Chem. Eng. 4 (2016) 1267–1273.
[29] J. Maragatha, S. Rajendran, T. Endo, S. Karuppuchamy, Microwave synthesis of metal doped TiO2 for photocatalytic applications, J. Mater. Sci.: Mater. Electron. 28 (2017) 5281–5287.
[30] J. Melcher, S. Feroz, D. Bahnemann, Comparing photocatalytic activities of commercially available iron-doped and iron-undoped aeroxide TiO2 P25 powders, J. Mater. Sci. 52 (2017) 6341–6348.
[31] N.u. Saqib, R. Adnan, I. Shah, A mini-review on rare earth metal-doped TiO2 for photocatalytic remediation of wastewater, Environ. Sci. Pollut. Res. 23 (2016) 15941–15951.
[32] N. Smirnova, I. Petrik, V. Vorobets, G. Kolbasov, A. Eremenko, Sol-gel synthesis, photo- and electrocatalytic properties of mesoporous TiO2 modified with transition metal ions, Nanoscale Res. Lett. 12 (2017) 239.
[33] S. Sood, A. Umar, S.K. Mehta, S.K. Kansal, Highly effective Fe-doped TiO2 nanoparticles photocatalysts for visible-light driven photocatalytic degradation of toxic organic compounds, J. Colloid Interface Sci. 450 (2015) 213–223.
[34] L.-T. Tseng, X. Luo, N. Bao, J. Ding, S. Li, J. Yi, Structures and properties of transition-metal-doped TiO2 nanorods, Mater. Lett. 170 (2016) 142–146.
[35] M.-C. Wu, T.-H. Lin, J.-S. Chih, K.-C. Hsiao, P.-Y. Wu, Niobium doping induced morphological changes and enhanced photocatalytic performance of anatase TiO2, Jpn. J. Appl. Phys. 56 (2017) 04CP07.
[36] M. Dong, P. Zhou, C. Jiang, B. Cheng, J. Yu, First-principles investigation of Cu-doped ZnS with enhanced photocatalytic hydrogen production activity, Chem. Phys. Lett. 668 (2017) 1–6.
[37] P. Zhou, J. Yu, Y. Wang, The new understanding on photocatalytic mechanism of visible-light response NS codoped anatase TiO2 by first-principles, Appl. Catal. B 142-143 (2013) 45–53.
[38] S.A. Ahmed, Structural, optical, and magnetic properties of Cu-doped TiO2 samples, Cryst. Res. Technol. 52 (2017) 1600335.
[39] P. Pongwan, K. Wetchakun, S. Phanichphant, N. Wetchakun, Enhancement of visible-light photocatalytic activity of Cu-doped TiO2 nanoparticles, Res. Chem. Intermed. 42 (2016) 2815–2830.
[40] C. Liu, J. Wang, W. Chen, Z. Sun, Z. Cao, Performance and mechanism of UV/Immobilized Cu-TiO2 system to degradation histidine, J. Nanomater. 2016 (2016) 9.
[41] B. Anitha, M.A. Khadar, Dopant concentration dependent magnetism of Cu-doped TiO2 nanocrystals, J. Nanopart. Res. 18 (2016) 149.
[42] Y. Li, X. Li, J. Li, J. Yin, Photocatalytic degradation of methyl orange by TiO2-coated activated carbon and kinetic study, Water Res. 40 (2006) 1119–1126.
[43] M.-C. Wu, P.-H. Lee, D.-L. Lee, Enhanced photocatalytic activity of palladium decorated TiO2 nanofibers containing anatase-rutile mixed phase, Int. J. Hydrogen Energy 40 (2015) 4558–4566.

[44] Y. Chimupala, G. Hyett, R. Simpson, R. Mitchell, R. Douthwaite, S.J. Milne, R.D. Brydson, Synthesis and characterization of mixed phase anatase TiO2 and sodium-doped TiO2(B) thin films by low pressure chemical vapour deposition (LPCVD), RSC Adv. 4 (2014) 48507–48515.
[45] A.L. Patterson, The scherrer formula for x-ray particle size determination, Phys. Rev. 56 (1939) 978–982.
[46] M.-C. Wu, J.-S. Chih, W.-K. Huang, Bismuth doping effect on TiO2 nanofibres for morphological change and photocatalytic performance, CrystEngComm 16 (2014) 10692–10699.
[47] F. Bensouici, M. Bououdina, A.A. Dakhel, R. Tala-Ighil, M. Tounane, A. Iratni, T. Souier, S. Liu, W. Cai, Optical, structural and photocatalysis properties of Cu-doped TiO2 thin films, Appl. Surf. Sci. 395 (2017) 110–116.
[48] M. Dorraj, M. Alizadeh, N.A. Sairi, W.J. Basirun, B.T. Goh, P.M. Woi, Y. Alias, Enhanced visible light photocatalytic activity of copper-doped titanium oxide–zinc oxide heterojunction for methyl orange degradation, Appl. Surf. Sci. 414 (2017) 251–261.
[49] T. Ohsaka, F. Izumi, Y. Fujiki, Raman spectrum of anatase, TiO2, J. Raman Spectrosc. 7 (1978) 321–324.
[50] V. Barron, J. Torrent, Use of the Kubelka—Munk theory to study the influence of iron oxides on soil colour, J. Soil Sci. 37 (1986) 499–510.
[51] M. Khairy, W. Zakaria, Effect of metal-doping of TiO2 nanoparticles on their photocatalytic activities toward removal of organic dyes, Egypt. J. Pet. 23 (2014) 419–426.
[52] V. Gombac, L. Sordelli, T. Montini, J.J. Delgado, A. Adamski, G. Adami, M. Cargnello, S. Bernal, P. Fornasiero, CuOx-TiO2 photocatalysts for H2 production from ethanol and glycerol solutions, J. Phys. Chem. A 114 (2010) 3916–3925.
[53] J. Fu, S. Cao, J. Yu, J. Low, Y. Lei, Enhanced photocatalytic CO2-reduction activity of electrospun mesoporous TiO2 nanofibers by solvothermal treatment, Dalton Trans. 43 (2014) 9158–9165.
[54] M.-C. Wu, J. Hiltunen, A. Sápi, A. Avila, W. Larsson, H.-C. Liao, M. Huuhtanen, G. Tóth, A. Shchukarev, N. Laufer, Á. Kukovecz, Z. Kónya, J.-P. Mikkola, R. Keiski, W.-F. Su, Y.-F. Chen, H. Jantunen, P.M. Ajayan, R. Vajtai, K. Kordás, Nitrogen-doped anatase nanofibers decorated with noble metal nanoparticles for photocatalytic production of hydrogen, ACS Nano 5 (2011) 5025–5030.